Revista Mexicana de Astronomía y Astrofísica, **58**, 133–153 (2022)
© 2022: Instituto de Astronomía, Universidad Nacional Autónoma de México
https://doi.org/10.22201/ia.01851101p.2022.58.01.11

TEMPERATURE DISCREPANCY WITH PHOTOIONIZATION MODELS OF THE NARROW-LINE REGION

Luc Binette[1], Montserrat Villar Martín[2], Gladis Magris C.[3], Mariela Martínez-Paredes[4], Alexandre Alarie[5], Alberto Rodríguez Ardila[6], and Ilhuiyolitzin Villicaña-Pedraza[7]

Received December 28 2021; accepted January 25 2022

ABSTRACT

Using published work on the narrow-line region of active galactic nuclei, a comparison is carried out among the [O III] λ4363Å/λ5007Å ($R_{\rm OIII}$) ratio observed in quasars, Seyfert 2's and the spatially resolved ENLR plasma. Using the weak [Ar IV] λ4711Å/λ4740Å doublet ratio observed by Koski (1978) among Seyfert 2's, we find evidence of a narrow-line region (NLR) populated by low density emission clouds ($\lesssim 10^4\,{\rm cm}^{-3}$). After considering calculations of the [Ar IV] and [O III] ratios that assume a power law distribution of plasma densities, no evidence of collisional deexcitation is found. The plasma temperature inferred is 13 500 °K, which is problematic to reproduce with standard photoionization calculations. The simplest interpretation for the near coincidence of the $R_{\rm OIII}$ ratios among the ENLR and Seyfert 2 measurements ($R_{\rm OIII} \simeq 0.017$) is that the low density regime applies to both plasmas.

RESUMEN

Utilizando trabajos publicados sobre la región de líneas angostas de los núcleos galácticos activos, se compara el [O III] λ4363Å/λ5007Å ($R_{\rm OIII}$) observado en cuásares, Seyfert 2 y en el plasma espacialmente resuelto de la ENLR. Mediante el débil doblete de [Ar IV] λ4711Å/λ4740Å observado por Koski encontramos evidencias de una región de líneas angostas (NLR) poblada por nubes de emisión de baja densidad ($\lesssim 10^4\,{\rm cm}^{-3}$). Tras considerar los cálculos de las relaciones [Ar IV] y [O III] que asumen una distribución de ley de potencia de las densidades del plasma, no se encuentra evidencia de desexcitación colisional. La temperatura del plasma que se infiere es de 13 500 °K, la cual es difícil de reproducir con los cálculos estándar de fotoionización. La interpretación más sencilla de la casi coincidencia de los cocientes de $R_{\rm OIII}$ medidos en la ENLR y las Seyfert 2 ($R_{\rm OIII} \simeq 0.017$) sería que el régimen de baja densidad se aplica a ambos plasmas.

Key Words: dust, extinction — galaxies: Seyfert — plasmas — quasars: emission lines

1. INTRODUCTION

The physics of the so-called narrow-line region of active galactic nuclei (AGN) has been amply studied (cf. Osterbrock 1978, and references therein). AGN emission line spectra can be divided into two categories[8]: Type I when the full width half-maximum (FWHM) of the permitted lines are significantly larger than the forbidden lines, and Type II where both the permitted and forbidden lines have similar FWHM. The broad-line region (BLR) observed in Type I objects originates from high density gas ($> 10^8\,{\rm cm}^{-3}$) much closer to the black-hole (BH) than the narrow-line region (hereafter NLR), the latter being observed in both Type I and II objects. The

[1]Instituto de Astronomía, UNAM, México.
[2]Centro de Astrobiología, Departamento de Astrofísica, Madrid, Spain.
[3]Centro de Investigaciones de Astronomía, Mérida, Venezuela.
[4]Korea Astronomy and Space Science Institute, Daejeon, South Korea.
[5]Département de physique, de génie physique et d'optique, Université Laval, Québec, Canada.
[6]Laboratório Nacional de Astrofísica, Itajubá, Brazil.
[7]DACC Science Department, New Mexico State University, USA.

[8]The current study does *not* include BL Lac objects nor extremely red quasars.

AGN unified model sustains that both types relate to the same phenomenon, with the differences being the visibility of the central engine. It proposes that the BLR is hidden from direct view in Type II due to an optically thick dusty torus-like gas structure surrounding the central engine (black hole, accretion disk, and BLR) (Antonucci 1993). Whether the BLR is observed or not depends on the viewing angle of the nucleus. Seyfert 2's, QSO 2's and narrow line radio galaxies (NLRG) are classified as Type II while Seyfert 1's, quasars, QSO 1's and broad-line radio galaxies (BLRG) are of Type I because their BLR is visible.

While it is customary to assume for H II regions the low density regime (hereafter LDR) when evaluating the plasma temperature using the [O III] λ4363Å/λ5007Å line ratio (hereafter labeled $R_{\rm OIII}$), this is inappropriate for the NLR, at least in Type I objects. Osterbrock (1978) interpreted the relative strength of the λ4363Å line, which was measured to be higher in Seyfert 1's and BLRG than in Seyfert 2's, as evidence of densities in the range $10^6 - 10^7\,{\rm cm}^{-3}$ within the NLR of Type I AGN. This interpretation was confirmed by the study of Baskin & Laor (2005, hereafter BL05) who compared the $R_{\rm OIII}$ they measured in 30 quasars. Their single-density calculations showed that the broad range of observed $R_{\rm OIII}$ ratios implies high plasma densities, ranging from possibly 10^5 up to $10^7\,{\rm cm}^{-3}$, providing convincing evidence of the important role of collisional deexcitation in Type I AGN, where the temperature cannot be directly inferred from the $R_{\rm OIII}$ ratio. In the case of Type II objects (Seyfert 2's and NLRG), the $R_{\rm OIII}$ ratio is on average smaller ($\lesssim 0.019$) although selection effects may possibly bias such an assessment. Prevailing NLR photoionization models consider a distribution of clouds that extends over a wide range of values of densities and ionization parameter, whether the targets are Type I (Baldwin et al. 1995; Korista et al. 1997) or Type II objects (Ferguson et al. 1997; Richardson et al. 2014). With respect to the spatially resolved emission line component of AGN, the so-called extended NLR (hereafter ENLR), it consists of *off-nuclear* line emission from plasma at typically LDR densities (e.g. Tadhunter et al. 1994; Bennert et al. 2006a,b) where the $R_{\rm OIII}$ ratio should provide a reliable temperature measurement.

The original element of the current work is the use of the weak [Ar IV] $\lambda\lambda$4711,40Å doublet to evaluate to what extent the $R_{\rm OIII}$ measurements of our selected Seyfert 2 sample is affected by collisional deexcitation. To cover the multi-density case, we developed an algorithm, OSALD, to calculate density and temperature line ratio *diagnostics* appropriate to isothermal plasmas in which the density follows a power law distribution rather than taking on a single value. This algorithm offers the option of including a foreground dust extinction component whose opacity, rather than being uniform, correlates with the emission plasma density. Our main conclusion is that (at least for the subset of Type II objects where the [Ar IV] doublet is observed) there is no evidence of significant collisional deexcitation. Hence, in those cases the $R_{\rm OIII}$ ratio constitutes a direct temperature indicator. Oddly, LDR photoionization calculations result in temperature discrepancies with the observations, underscoring the so-called temperature problem (Storchi-Bergmann et al. 1996; Bennert et al. 2006a; Villar-Martín et al. 2008; Dors et al. 2015, 2020). In a follow-up paper, we evaluate different physical processes to address this issue.

Our reference sample is described in § 2 and a comparison with single-component photoionization models is presented in § 3. A modified interpretation of the NLR $R_{\rm OIII}$ ratios observed near $\simeq 0.017$ in Type II and some Type I AGN is proposed in § 4. These are subsequently compared with calculations made with the algorithm OSALD (§ 5), which considers a power law density distribution.

2. REFERENCE DATA SET OF $R_{\rm OIII}$ RATIOS IN AGN

In what follows, the term NLR will be used exclusively in reference to the spatially *unresolved* nuclear component. For any line emission that originates beyond the spatially unresolved central component[9] of the active nucleus, it will be referred as ENLR[10] in all cases where the gas is deemed photoionized by the AGN rather than by hot stars.

In order to evaluate the impact of collisional-deexcitation on the [O III] emission lines among Type I and II AGN, our data set consists primarily of the quasar sample of BL05 (excluding upper limits data), to which we added the four narrow-line Seyfert 1 studied by Rodríguez-Ardila et al. (2000a, hereafter RA00) which were originally observed by Rodríguez-Ardila et al. (2000b). To have access to measurements of the $\lambda\lambda$4711,40Å doublet, we relied

[9] Where the densest plasma of the BLR and inner NLR is located.

[10] When the line emission lies kiloparsecs or more away from the nucleus, some authors (e.g., Tadhunter et al. 1988) prefer the term extended emission line region (EELR).

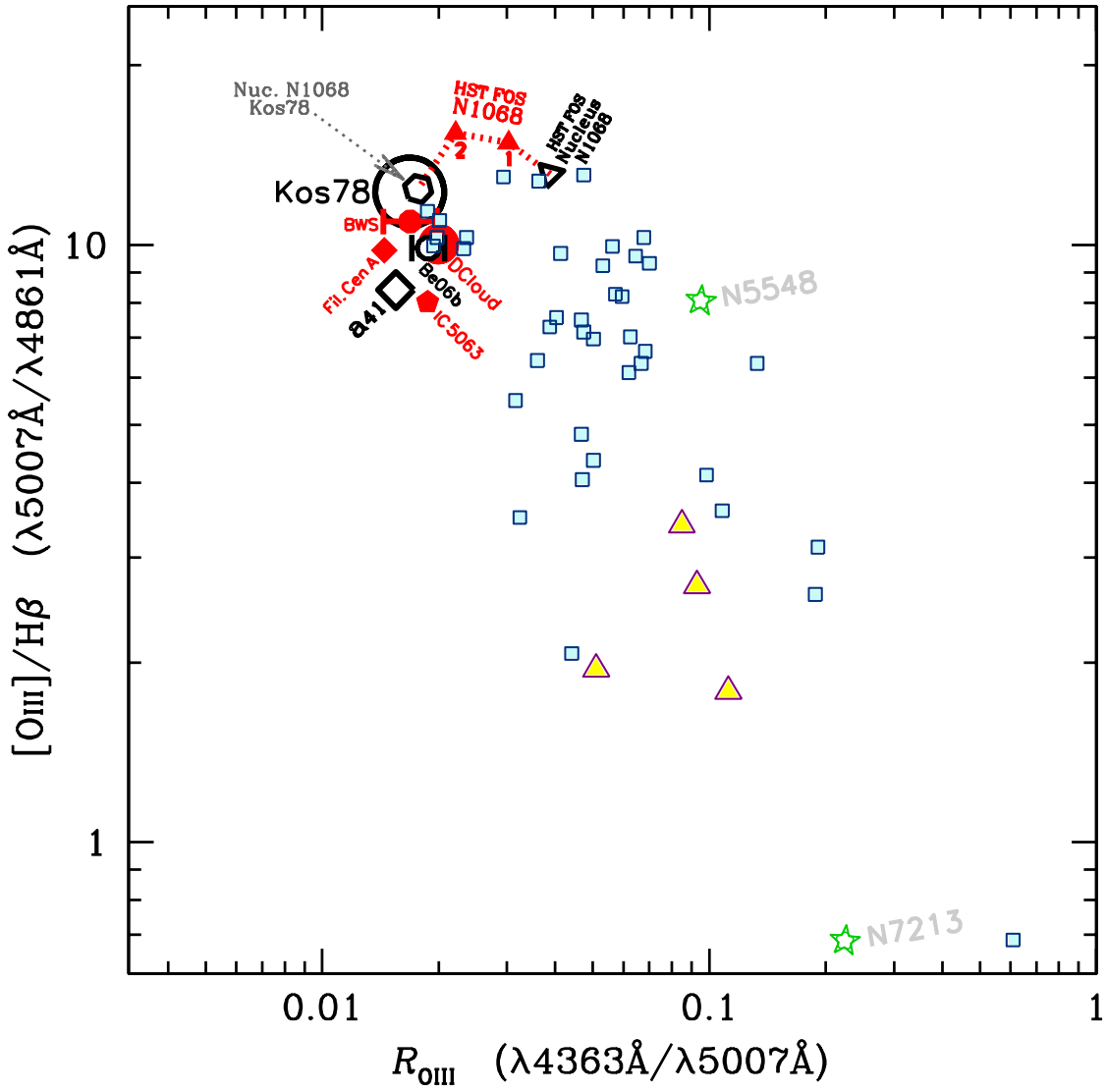

Fig. 1. AGN dereddened line ratios of [O III]/Hβ vs. $R_{\rm OIII}$ from: A- Type I AGN with measurements of (1) 30 quasars studied by BL05 (bluish open squares), (2) four narrow-line Seyfert 1 galaxies from RA00 (yellowish open triangles), (3) two Seyfert 1.5, NGC 5548 and NGC 7213 (open stars), B-Type II AGN represented by open *black* symbols consisting of (1) the average of seven Seyfert 2's from Kos78 (large circle), (2) the average of four Seyfert 2's from Be06b (small circle), (3) the high excitation Seyfert 2 subset a41 from Ri14 (diamond), (4) the nucleus of NGC 1068 through ground-based observations by Kos78 (black hexagon) and HST-FOS observations analysed by Kr98 (black open triangle), and C- ENLR measurements (all as red filled symbols) consisting of (1) the average from BWS of two Seyfert 2's and two NLRGs (red dot), (2) the long-slit observations of the Seyfert 2 IC 5063 by Be06b (pentagon), (3) the average of seven spatially resolved optical filaments from the radio-galaxy Centaurus A (red square) by Mo91, (4) the 8 kpc *distant cloud* from radiogalaxy Pks 2152−699 by Ta87 (large dot), and (5) the HST-FOS measurements of two ENLR knots from NGC 1068 (red triangles). The colour figure can be viewed online.

on the Seyfert 2 sample of Koski (1978, hereafter Kos78). Finally, to ensure that our sample covers cases where the emission plasma is negligibly affected by collisional deexcitation, we included diverse ENLR observations from the literature. Figure 1 describes the behaviour of the dereddened [O III]/Hβ (λ5007Å/λ4861Å) and $R_{\rm OIII}$ (λ4363Å/λ5007Å) line ratios of our AGN sample.

TABLE 1

REDDENING-CORRECTED SEYFERT 2 RATIOS FROM KOSKI (1978)

(1) Index #	(2)[a] Seyfert 2	(3) [O III]/Hβ $\frac{\lambda 5007}{\lambda 4861}$	(4) $R_{\rm OIII}$ $\frac{\lambda 4363}{\lambda 5007}$	(5) [Ar IV]$_+$ $\frac{\lambda 4711+}{\lambda 4740}$	(6) $R_{\rm He/Ar}$ $\frac{\lambda 5876}{\lambda 4740}$	(7)[b] $f^{HeI}_{\rm blend}$	(8)[c] $n_{\rm sng}$ cm^{-3}	(9)[d] $T^{sng}_{\rm OIII}$ °K
1	Mrk 573	12.12	0.0149	1.167	1.52	0.039	1.85×10^3	13 360
2	Mrk 34	11.46	0.0131	1.203	2.03	0.051	1.64×10^3	12 720
3	Mrk 78	11.94	0.0117	1.267	2.22	0.053	1.14×10^3	12 210
4	Mrk 176	14.36	0.0223	1.045	0.45	0.013	2.84×10^3	15 940
5	Mrk 3	12.67	0.0189	0.837	1.95	0.072	7.21×10^3	14 670
6	Mrk 1	10.95	0.0192	0.825	1.59	0.059	7.25×10^3	14 760
7	NGC 1068	12.42	0.0177	0.790	2.42	0.097	8.77×10^3	14 210

[a]The line ratios from the 7 Seyfert 2's were reddening corrected by Koski (1978) using the observed Balmer decrement. The measurement uncertainties were estimated at ±10% for the strong line fluxes and ±20% for the weak lines.

[b]The inferred fractional contribution of He I λ4713Å to the blended λ4711Å$_+$ line.

[c]The densities $n_{\rm sng}$ were determined using the deblended λ4711Å/λ4740Å doublet ratio.

[d]The temperature $T^{sng}_{\rm OIII}$ was derived from the $R_{\rm OIII}$ ratio assuming the density $n_{\rm sng}$ inferred from the deblended [Ar IV] ratio (see § 5.1.5). The average temperature from Column (7) is $\langle T^{sng}_{\rm OIII} \rangle = 13\,980 \pm 1200$ °K.

2.1. *Detailed Description of the Dereddened $R_{\rm OIII}$ Data Set*

The data set was extracted from the following sources:

A – NLR of Type I AGN

(a) Based on the prominent work of BL05, the sample consists of 30 Type I quasars with $z < 0.5$, mostly from the bright quasar survey of Boroson & Green (1992). Objects where only upper limits of [O III] λ4363Å were reported have been excluded. The sample is represented by bluish open squares in Figure 1. The authors used the [O III] λ5007Å profile of each object as template for extracting the NLR Hβ and [O III] λ4363Å line fluxes. Since the latter line is weak, its measurement required a proper subtraction of the underlying Fe II emission multiplets. BL05 used the I Zw 1 Fe II template provided by T. Boroson (private communication) to subtract the Fe II multiplets. All the line fluxes were corrected for dust reddening and possible slit losses.

(b) The measurements of the four narrow-line Seyfert 1 nuclei (hereafter NLS1) from RA00 (yellowish open triangles) were annexed. As detailed in their study, the authors used their own spectrum of I Zw 1 to subtract the various Fe II underlying features present in their NLS1 spectra. They compared different ways to extract the Hβ NLR contribution, favouring in the end the procedure of fitting a narrow and broad Gaussian component to the Hβ profiles. The broad to narrow Hβ flux ratios in these objects cover the range of 1.8 to 3.4.

(c) For comparison purposes, we included the measurements of two well-studied Seyfert 1.5 galaxies (light-green open stars): NGC 5548 (Kraemer et al. 1998a) and NGC 7213[11] (Filippenko & Halpern 1984).

B – NLR of Type II AGN

(a) To characterize the behaviour of high excitation Type II objects, we adopt the pioneering work on Seyfert 2's by Koski (1978, hereafter Kos78), which provides the unique characteristic of reporting reliable measurements of the weak [Ar IV] $\lambda\lambda$4711,40Å doublet ratio, an essential density indicator for evaluating in § 4.2 and § 5.2 to what extent the observed $R_{\rm OIII}$ is affected by collisional deexcitation. Table 1 lists the reddening corrected ratios of the

[11]Initially associated to the LINER category, the presence of [Ne V] lines indicates a high ionization plasma despite having [O III]/H$\beta < 1$ due to collisional deexcitation.

high excitation subset of their sample (i.e. with [O III]/Hβ $\geq$ 10), which consists of seven Seyfert 2's. Two objects, Mrk 348 and 3C33, were left out of Table 1 since their measurement of the [Ar IV] ratio unrealistically exceeded the low density limit value. They presumably indicate emission from LDR plasma. The average $R_{\rm OIII}$ ratio from Table 1 is 0.0168 (i.e. $10^{-1.77}$ in Figure 1), which is represented by a large black disk whose radius of 0.088 dex corresponds to the $R_{\rm OIII}$ RMS dispersion. The average [O III]/Hβ is 12.3 ± 1.1.

(b) As a complement to Type II objects, we averaged the measurements of the four Seyfert 2's IC 5063, NGC 7212, NGC 3281 and NGC 1386 observed by Bennert et al. (2006b, hereafter Be06b). It is represented by a small black circle corresponding to a mean $R_{\rm OIII}$ of 0.0188. Pseudo error bars represent the RMS dispersion of 0.042 dex.

(c) The black diamond labelled a41 with $R_{\rm OIII} = 0.0155$ represents the high ionization end of the sequence of reconstructed spectra of Richardson et al. (2014, hereafter Ri14) which was extracted from a sample of 379 AGN. These were identified by applying the Mean Field Independent Component Analysis (MFICA) tool to their Sloan Digital Sky Survey (SDSS) sample of $\approx 10^4$ emission line galaxies in the redshift range $0.10 < z < 0.12$ (see also Allen et al. 2013). They meticulously reviewed each spectrum to ensure that no BLR component was present.

(d) Ground-based observations of the Seyfert 2 NGC 1068 nucleus by Kos78 is represented by the black open octagon while the black open triangle corresponds to the HST-FOS measurement of the nucleus at a much higher spatial resolution of $0.3\widehat{''}$ (archive data Kraemer et al. 1998b, hereafter Kr98).

C – Spatially resolved ENLR emission

(a) The red filled dot stands for the average ratio from the ENLR of four Type II AGN (two are Seyfert 2's: ESO 362-G08 and MRK 573, and two are NLRGs: Pks 0349−27 and Pks 0634−20) which were studied by Storchi-Bergmann et al. (1996, hereafter SB96). The mean $R_{\rm OIII}$ ratio is 0.0169 ± 0.0029, which includes measurements on both sides of the nucleus, except for ESO 362-G08 (Binette et al. 1996, hereafter BWS). Pseudo-error bars denote an RMS dispersion of 0.07 dex.

(b) The Seyfert 2 IC 5063. The red pentagon represents the average ratio $R_{\rm OIII} = 0.0188$ (with dispersion of 0.042 dex) from the *extranuclear* radial emission of the Seyfert 2 IC 5063 which Be06b observed with a $S/N > 3$ from $8\widehat{''}$ NW to $5\widehat{''}$ SE.

(c) The Centaurus A (NGC 5128) filaments. The red square represents the average ratio of seven optical filaments studied by Morganti et al. (1991, hereafter Mo91) and situated along the radio jet at a mean distance of 490 pc from the nucleus of the radio-galaxy Centaurus A (mean $R_{\rm OIII} = 0.0145$ with a dispersion of 0.13 dex).

(d) Detached cloud emission aligned with radio-galaxy jets. The large red dot represents the well studied 8 kpc distant cloud associated to the nucleus of radiogalaxy Pks 2152−699 (Tadhunter et al. 1987, hereafter Ta87).

(e) Two detached emission line 'knots' of NGC 1068 labelled 1 and 2 (red triangles) which were studied by Kr98 using HST-FOS archive data. The positions are off-centered from the nucleus by $0.2\widehat{''}$ and $0.7\widehat{''}$, respectively.

3. PHOTOIONIZATION CALCULATIONS AT LDR DENSITIES

All our calculations will be presented in Figure 3 in which the reference data set is represented using the same symbols but coloured in gray. For an isothermal plasma at a fixed temperature, densities much above LDR would cause an increase of the $R_{\rm OIII}$ ratio, shifting its position to the right in Figure 3 due to collisional deexcitation. The segmented cyan arrow describes the increase in $R_{\rm OIII}$ expected from a 14 000 °K plasma slab whose density successively takes on the values of 10^2 (LDR), $10^{4.5}$, 10^5, $10^{5.5}$, 10^6 and $10^{6.5}$ cm^{-3}. It illustrates the density range implied by the BL05 and RA00 Type I AGN if they shared the same temperature. For a 15 000 °K plasma, the critical densities[12] for deexcitation of

[12] We define the critical density as the density where the line intensity, divided by both the ion and the electron densities, reaches 50% of the low density limit value.

the [O III] λ5007Å and λ4363Å lines are 7.8×10^5 and $2.9 \times 10^7\,\mathrm{cm}^{-3}$, respectively, while for the[Ar IV] λ4711Å and λ4740Å lines these are 1.7×10^4 and $1.5 \times 10^5\,\mathrm{cm}^{-3}$. Let us compare the data with the values predicted by photoionization calculations.

3.1. *Above Solar Gas Metallicities*

The abundances we adopt correspond to $2.5\,Z_\odot$, a value within the range appropriate to galactic nuclei of spiral galaxies. For instance, the landmark study by Dopita et al. (2014) of multiple H II regions of the Seyfert 2 NGC 5427 favour abundances significantly above solar. Using the Wide Field Spectrograph (WiFeS: Dopita et al. 2010), the authors could determine the ISM oxygen radial abundances using 38 H II regions spread between 2 and 13 kpc from the nucleus. Using their inferred metallicities, they subsequently modelled the line ratios of over 100 'composite' ENLR-H II region emission line spaxels, as well as the line ratios from the central NLR. Their highest oxygen abundance reaches $3\,Z_\odot$ (i.e. $12 + \log(\mathrm{O/H} = 9.16)$. Such a high value is shared by other observational and theoretical studies that confirm the high metallicities of Seyfert nuclei (Storchi-Bergmann & Pastoriza 1990; Nagao et al. 2002; Ballero et al. 2008). Our abundance set relative to H corresponds to twice the solar values of Asplund et al. (2006) except for C/H and N/H, which are set at four times the solar values owing to secondary enrichment, resulting in a gas metallicity of $Z_{\rm tot} = 2.47 Z_\odot$ by mass. For the He/H abundance ratio, we assume the solar value of 0.085.

3.2. *Four Alternative Ionizing Energy Distributions*

The four spectral energy distributions (hereafter SED) selected are shown in Figure 2. They are representative of published work concerning AGN photoionization models and can be described as follows:

A: the long dashed-line represents the SED used by Ferguson et al. (1997, hereafter Fg97) in their calculations of local optimally emitting cloud (LOC) models for the NLR. It is characterized by a thermal bump of the form

$$F_\nu \propto \nu^{\alpha_{UV}} \exp(-h\nu/kT_{cut}),$$

with $\alpha_{UV} = -0.3$ and $T_{cut} = 10^{6.0}$ °K.

B: the dot-dashed line represents the 'optimized SED' used by Richardson et al. (2014, hereafter Ri14) in their calculations of LOC models. It shares the same index α_{UV} as the Fg97 SED above, but assumes a lower T_{cut} of $10^{5.52}$ °K to describe the thermal bump. It is significantly softer than the Fg97 SED, yet due to collisional deexcitation being important in LOC models, these qualitatively reproduces the $R_{\rm OIII}$ and He II/Hβ (λ4686Å/λ4861Å) ratios of their reconstructed Seyfert 2 emission line spectra.

C: a power law of index $\alpha_{FUV} = -1.3$ in the far-UV domain (continuous black line) which was used by Binette et al. (1996, hereafter BWS) and Binette et al. (1997) in their matter-bounded cloud calculations.

D: the thick continuous gray line represents the sum of two distinct thermal bumps as proposed by Lawrence (2012, hereafter La12) who postulated that the accretion is entirely covered by intervening thick BLR clouds, which would absorb Ly α as well as the softer ionizing radiation, thereby accounting for the observed UV steepening short-ward of 1050Å. The author proposed that the absorbed EUV energy is re-

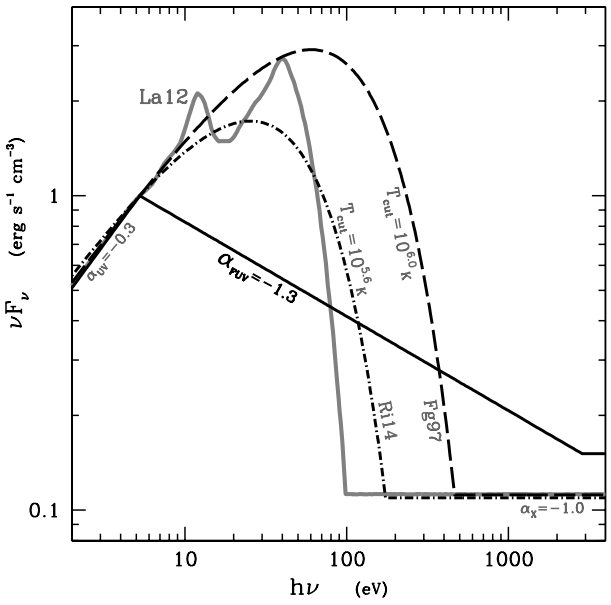

Fig. 2. The four SEDs described in § 3 and adopted in our LDR single-component photoionization models of Figure 3: (1) the SED assumed by Ri14 with $T_{cut} = 10^{5.62}$ °K in their LOC model calculations (dot-dashed line), (2) a similar SED but with a higher T_{cut} of $10^{6.0}$ °K as explored by Fg97 (long dashed-line), (3) a power law SED with $\alpha_{FUV} = -1.3$ adopted by BWS (black continuous line), (4) the double bump thermal SED proposed by La12 (thick gray line). Each SED is expressed in νF_ν units and normalized to unity at 5 eV (2000Å). In the X-rays, they all convert into a power law of index −1.0.

processed into emission at much shorter wavelengths, which generates the second peak near 40 eV.

Each SED converts in the X-rays into a power law $F_\nu \propto \nu^{-1}$ and results in an α_{OX} index[13] of −1.35 except the BWS SED ($\alpha_{OX} = -1.30$).

3.3. *Isochoric Single-Component Photoionization Calculations*

Sequences of photoionization models are shown in Figure 3 corresponding to the four SEDs of Figure 2. LDR was assumed as it is the appropriate density regime for the ENLR plasma and for at least a significant subset of the AGN sample, as argued in § 4. They were calculated using the most recent [14] version Ig of the code MAPPINGS I (Binette et al. 2012) All models share the same density of $n_H^o = 100\,\mathrm{cm}^{-3}$ and each sequence includes up to six models[15] along which the ionization parameter $\mathrm{U_o}$ increases in steps of 0.33 dex, from 0.01 (gray dot) up to 0.46. A filled square denotes the $\mathrm{U_o} = 0.1$ model. All calculations are ionization-bounded, dustfree and isochoric. The observational data set represented in Figure 3 uses only black or gray tones but with the same symbol coding as in Figure 1.

If we define the photoheating efficiency of each SED as the temperature of the plasma averaged over the region occupied by the O^{+2} ion, we obtain for the $\mathrm{U_o} = 0.1$ model the following values of 11 300, 9700, 8400 and 8320 °K, assuming the SED which we labelled BWS, Fg97, La12 and Ri14, respectively (Figure 3). The BWS SED possesses the highest efficiency but it is more speculative as it excludes the possibility of thermal dump (or peak) in the far-UV. Such a feature is to be expected if the continuum originates from an accretion disk, which is widely accepted as being the primary mode of energy generation in AGN. The double-peak reprocessed SED of La12 presents the advantage of accounting for the 'universal' knee observed at 10 eV. The position of the second peak at 40 eV, however, would need to be shifted to higher energies in order to increase the photoheating efficiency.

It is currently not possible to determine which abundances are the most appropriate to the environment of active nuclei although it is generally accepted that metallicities above solar are most likely. If one assume the more conservative metallicity of $1.5\,Z_\odot$ of Fg97 and Ri14, a shift towards the right takes place, as shown by the dotted line arrows in Figure 3, assuming an ionization parameter of $\mathrm{U_o} = 0.1$.

What is the origin of the gap between the photoionization models and AGN observations? The positions of models on the left of Figure 3 correspond to LDR conditions. It is a justified option for the ENLR, as argued in Appendix A. As shown by BL05 as well as by the density sequence using the BWS SED in Figure 3 (gray dotted line), all models can be shifted towards higher R_{OIII} values by assuming plasma densities much above $10^{4.3}\,\mathrm{cm}^{-3}$. This is the main reason why direct measurements of the density governing the [O III] lines are so important if we wish to determine the NLR temperature. Measurements of the weak [Ar IV] doublet can give us access to this information, as explored below.

4. MIGHT THE AGN BUILDUP NEAR $R_{\mathrm{OIII}} \simeq 0.018$ REPRESENT A FLOOR TEMPERATURE?

The work of BL05 presented convincing evidence that the quasars (open squares) with R_{OIII} reaching ≈ 0.2 are the manifestation of collisional deexcitation from high density plasma. Their single-density photoionization calculations suggest densities of $\simeq 10^{6.5}\,\mathrm{cm}^{-3}$. Interestingly, the four quasars on the extreme left appear to clump at $R_{\mathrm{OIII}} = 0.0195$ with [O III]/Hβ $\simeq 10.5$ in Figure 3. At this position, single-density photoionization calculations from BL05 suggest densities near $10^{5.2}\,\mathrm{cm}^{-3}$. If we consider an isothermal 14 000 °K plasma (c.f. cyan arrow), the density we infer is very close to LDR, at $10^{3.3}\,\mathrm{cm}^{-3}$. Our initial analysis of R_{OIII} among Seyfert 2 galaxies indicated that these show R_{OIII} values similar to the leftmost quasars, which made us question whether collisional deexcitation is related to their position in Figure 3. Our analysis of the NLR data of Seyfert 2 galaxies, however, lead us to question whether collisional deexcitation is related to the position of these quasars on the left. It is noteworthy that, for instance, a similar position is occupied by: (1) the sample of four Seyfert 2 nuclei of Be06b (dark-green dot), (2) the reconstructed Seyfert 2 subset a41 from Ri14 (black diamond) which is based on an ample sample of SDSS spectra, and (3) the seven high excitation Seyfert 2's of Kos78, as shown by the black disk, which represents the average R_{OIII}. We

[13] Defined by the flux ratio at 2 keV with respect to 2500Å.

[14] This version includes the new algorithm OSALD (Appendix C.3). Other updates are described in a subsequent paper (Binette & Humphrey 2022).

[15] Some of the leftmost models of La12 and Ri14 fall outside the graph boundaries.

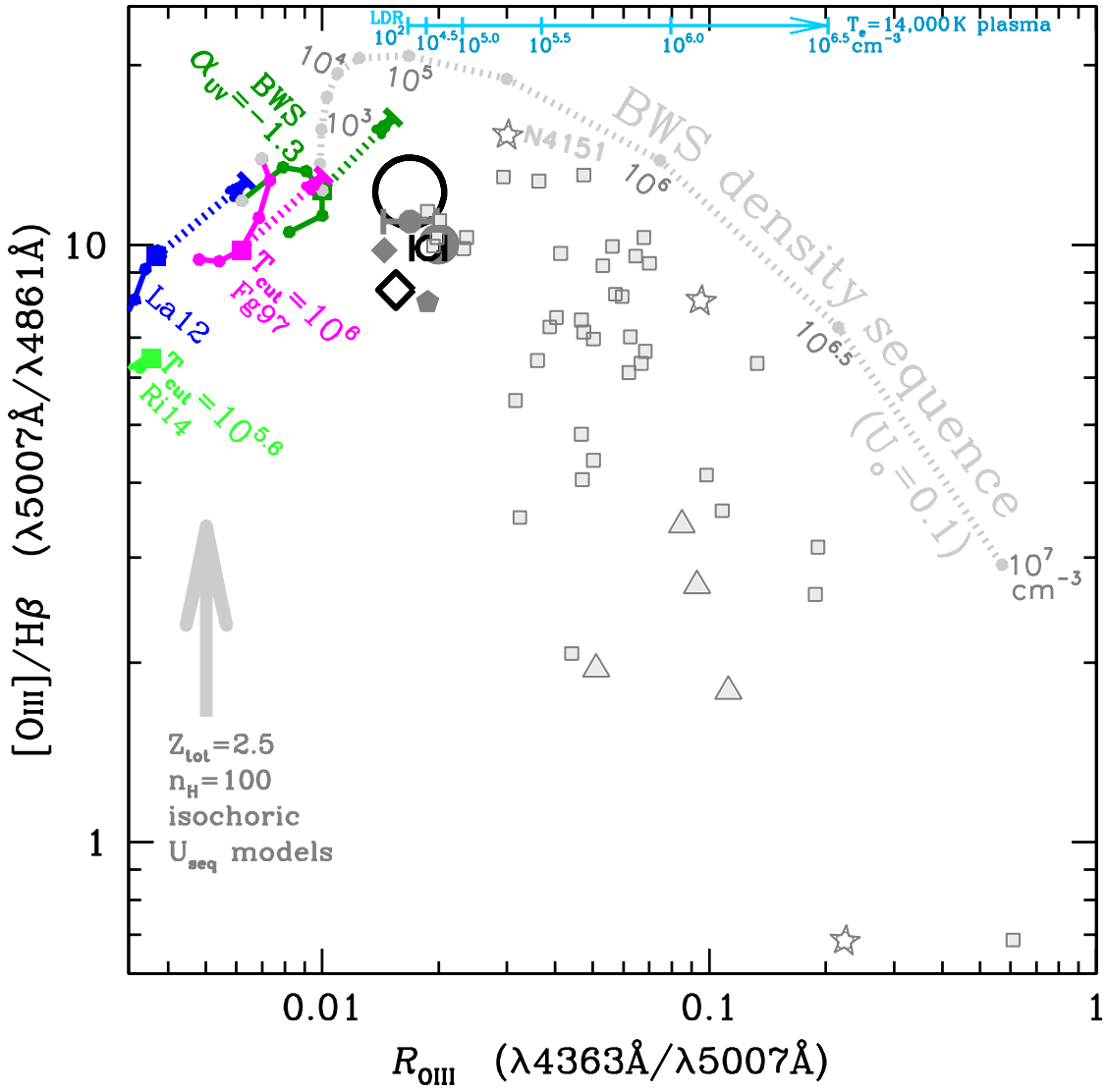

Fig. 3. Same data set from Figure 1 except that it now includes the Seyfert 1 NGC 4151 (c.f. § 5.2.3) instead of NGC 1068. The gray open symbols correspond to the NLR from Type I objects, black symbols to Type II and gray filled symbols to ENLR measurements. Four sequences of LDR photoionization models are shown (solid lines) along which the ionization parameter U_o increases in steps of 0.5 dex, from 0.01 (light gray dot) up to 0.46. Some models fall outside the figure limits. The sequences are labelled according to the SED defined in § 3.2: (A) Fg97 (magenta), (B) Ri14 (light green), (C) BWS (dark green) and (D) La12 (blue). The models are all ionization bounded, dustfree, isochoric with $n_H^o = 100\,\mathrm{cm}^{-3}$and $2.5\,Z_\odot$ abundances. A square identifies the $U_o = 0.1$ model with a dotted arrow representing the shift when one adopts the $1.5\,Z_\odot$ abundances of Ri14. The gray dotted line represents a density sequence in which the densities of the BWS model with $U_o = 0.1$ are successively increased in steps of 0.5 dex. The cyan segmented arrow at the top illustrates the effect of collisional deexcitation on the R_{OIII} ratio from a 14 000 °K plasma at successively larger densities. The colour figure can be viewed online.

would argue that the accumulation of AGN on the left is most likely representing a floor AGN temperature where collisional deexcitation is not significant. To support our hypothesis, we will make use in § 4.2 of the density indicator provided by the λ4711Å/λ4740Å doublet ratios of Kos78.

4.1. *Why do ENLR Observations Coincide with the Leftmost NLR R_{OIII} Observations?*

Because ENLR emission operates in the low density regime (c.f. Appendix A), it provides ideal measurements to compare Type II objects with. In

Figure 1, we added the following spatially resolved ENLR emission measurements: (1) the Cen A filaments (red square, Mo91), (2) the average ENLR ratios of four Type II AGN (red dot, BWS), (3) the radial ENLR emission from the Seyfert 2 IC 5063 (red pentagon: Be06b), and (4) the ionized cloud 8 kpc distant from of Pks 2152-69 (large red dot, Tadhunter et al. 1987). All gather relatively close to the leftmost Type I quasars (open squares) as well as to the mean Seyfert 2 ratio of the Kos78 study (large black circle). Interestingly, the Seyfert 2 reconstructed subset a41 (black diamond) of Ri14 occupies a similar position. The simplest interpretation would be that collisional deexcitation is *not* significant, not only within the spatially resolved ENLR but among the leftmost objects as well, and that they all share a similar electronic temperature.

4.2. *Combination of the [Ar IV] and [O III] Diagnostics*

To evaluate the NLR density, we will rely on the observations of Kos78 who measured the weak [Ar IV] $\lambda\lambda$4711,40Å doublet of his Seyfert 2 sample, an unusual feature among AGN surveys. The observations were carried out with the image-dissector-scanner mounted on the 3 m Shane telescope at the Lick Observatory. The integration times were typically 32 min (A. T. Koski, PhD thesis 1976). In Columns (3–4) of Table 1, we present the reddening-corrected line ratios of [O III]/Hβ and $R_{\rm OIII}$. In the context of high excitation planetary nebulae, Kewley et al. (2019) pointed out that the [Ar IV] and [O III] emission regions significantly overlap and that their respective ratios can be considered representative of the high excitation plasma. A concern, however, is that the weak He I λ4713Å line lies very close to the [Ar IV] λ4711Å line. Given the much wider profiles of the NLR lines in comparison to planetary nebulae, both lines will overlap. Hence the need to apply a deblending correction. The procedure we adopted for the single-density case is described in Appendix B.1. It essentially makes use of the dereddened He I λ5876Å line (Column 6) to calculate a reliable estimate of the contribution of the He I λ4713Å line to the blended[16] [Ar IV]$_+$ λ4711Å$_+$/λ4740Å doublet ratio (Column 5). The estimated fractional contribution of the blended He I line to [Ar IV]$_+$ is $f^{HeI}_{\rm blend}$ (Column 7), which amounts to 5% on average. NGC 1068 stands out at a higher value of 10%. For each object we iteratively determine which density $n_{\rm sng}$ is implied by the deblended [Ar IV] doublet ratio when it is calculated at the temperature $T^{sng}_{\rm OIII}$ which reproduces the $R_{\rm OIII}$ ratio. The inferred density values, $n_{\rm sng}$, given in Column (8), all lie below $10^4\,{\rm cm}^{-3}$. As indicated by the cyan arrow in Figure 3, the $R_{\rm OIII}$ ratio is not significantly affected by collisional deexcitation at densities below $10^4\,{\rm cm}^{-3}$. Taken at face values, the densities of Table 1 indicate that $R_{\rm OIII}$ is a valid temperature indicator for the Seyfert 2's of Kos78. The average temperature characterising the whole sample is $13\,980 \pm 1200$ °K, which lies significantly above the predictions of the LDR photoionization models of § 3.3. Rather than assuming a single density, in § 5 we will consider the case of a smoothly varying density distribution.

[16] The sub-index + sign denotes a line that incorporates a blended component from a different ion. The double $\lambda\lambda$ symbol refers to two separate but nearby lines of the same ion.

4.3. *Density Bias due to a Limited Spatial Resolution*

In Type I AGN, due to the favorable orientation of the observer with respect to the ionizing cone (Antonucci 1993), the densest NLR components are visible and possibly dominate the integrated line flux, causing the $R_{\rm OIII}$ ratios to occupy values up to 0.2 due to collisional deexcitation, as proposed by BL05.

In Type II AGN on the other hand, since the inner regions occupied by the accretion disk and the BLR are not visible, important selection effects take place. The NLR is likely not fully observed due to obscuration associated to the ionizing cone. Differences in spatial resolution as a result of the object distance and the size of the spectrograph aperture inevitably affect the sampling of the NLR volume. The angular resolutions characterising our Seyfert 2 sample are the following. The reconstructed NLR spectrum of Ri14 was based on SDSS observations of Seyfert 2's of similar redshifts (0.10 – 0.12) with a fiber aperture size of $3\widehat{''}$. This corresponds to a NLR sampling that extends over 5.6 kpc diameter. The nearest AGN of the Kos78 sample is NGC 1068 at $z = 0.0038$, which is discussed in detail below. The other objects have redshifts in the range 0.0135 to 0.051 which, for an aperture of $2.7\widehat{''} \times 4\widehat{''}$, result in angular sizes in the range $\simeq 1$ to 4 kpc at the object distance. The Be06b sample presents the highest spatial resolution since its four Seyfert 2's are of low redshift (0.003 – 0.027) and were observed with a seeing $\lesssim 1\widehat{''}$ using longslit spectroscopy mounted on the NTT and VLT telescopes of the European Southern Observatory. The slit aperture was $\simeq 1.1\widehat{''} \times 1\widehat{''}$, which translates into a NLR angular size of 50 to 600 pc. We might conjecture that such superior spatial resolution is possibly related to the position of

the Be06b sample in Figure 1, which is slightly more to the right than the Kos78 and Ri14 samples.

Unlike the BL05 quasar sample where collisional deexcitation is the evident cause of the wide spread of $R_{\rm OIII}$ values, the NLR of Seyfert 2's appears relatively unaffected by deexcitation, at least among ground-based observations. The much superior resolution from HST observations, however, reveals the presence of much denser components within the inner nucleus. A case in point are the HST-FOS observations of NGC 1068 (Kr98) with an angular resolution of $0.3\widehat{''}$ (i.e. 25 pc). The nucleus (black open triangle), for instance, shows an $R_{\rm OIII}$ ratio higher by a factor of two with respect to the ground-based observation of Kos78 (black octagon). The image of the nucleus in [O III] light using the HST-FOC instrument shows a diffuse underlying emission component that extends beyond 200 pc from the nucleus and which encompasses a number of emission knots of sizes $\gtrsim 10$ pc. Two bright (EELR) emission 'knots', labelled 1 and 2 by Kr98 (red filled triangles) observed with the $0.3\widehat{''}$ aperture show $R_{\rm OIII}$ values that fall between those of Kos78 (octagon) and of Kr98 with HST-FOS (open triangle). A red dotted line connects the four measurements in Figure 1. The two knots are situated at distances from the nucleus of 0.2 and $0.7\widehat{''}$, respectively (i.e. at 16 and 57 pc).

5. MULTI-DENSITY TEMPERATURE AND DENSITY DIAGNOSTICS

We expanded the functionality of the $R_{\rm OIII}$ temperature *diagnostic* by combining the latter with the [Ar IV] density indicator, allowing us to evaluate the impact of collisional deexcitation among the observed $R_{\rm OIII}$ ratios. To this effect, we developed the algorithm OSALD (see Appendix C for further information), which integrates the line emissivities from an isothermal plasma that extends over a wide density range, up to a cut-off density, $n_{\rm cut}$. At a given temperature, if $n_{\rm cut}$ has a high value, the integrated $R_{\rm OIII}$ ratio rises above the LDR value. Since our diagnostics depends on measurements of the [Ar IV] doublet, we are limited to the Kos78 sample of Table 1.

We have explored two options concerning the nature of the density cut-off: (1) that it simply consists of a sharp cut-off, or (2) corresponds to a gradual cut-off due to a foreground dust extinction layer whose opacity correlates with plasma density. The calculations assuming the first option are summarised in Appendix E and result in essentially the same temperatures as derived from the single density case explored in § 4.2. We will now consider the second option, where we explore the possibility that the NLR emission becomes gradually more absorbed towards the nucleus.

5.1. *Components of the Dust Screen Approach with* OSALD

One particularity of our proposed approach is that it implies fitting the *observed* $R_{\rm OIII}$ ratios presented in Table 2 rather than the dereddened ratios of Table 1 and Figure 1.

5.1.1. *A Density Cut-Off Generated by a Dust Extinction Gradient*

The dust opacity is described by an exponential function of density n: $\tau_V = \tau_V^o \exp(n/n_{\rm opa})$, where $n_{\rm opa}$ is the e-folding density that defines the gradual increase of the foreground V-band dust opacity towards the inner nucleus. This definition does not require us to distinguish between the Galactic extinction from that from the NLR dust screen (τ_V^o includes both). Our interest in exploring an ascending extinction towards the denser NLR component is motivated by the accumulating evidence of the importance of the orientation of the NLR (and not just of the BLR) with respect to the observer, as reviewed in Appendix D, and which is presumably the result of a cone-like opacity distribution.

5.1.2. *Extinction Curve and Line Transfer Algorithm*

The line transfer algorithm implemented in OSALD fully takes into account the effect of multiple scattering across the foreground dust layers. Its characteristics are described in Appendix C of Binette et al. (1993). As for the extinction curve, we adopt the one inferred by Martin & Rouleau (1991) in their study of the Orion nebula, which differs from the standard ISM curve in that grains of size smaller than 0.05 μm are absent, resulting in a flatter curve with less extinction in the UV (Baldwin et al. 1991; Magris C. et al. 1993). It is qualitatively in line with the evidence presented by Maiolino et al. (2001a,b) that small grains are depleted in the dusty medium which is responsible for the absorption of the X-rays and the reddening of the BLR lines. The V-band dust opacity τ_V^o is determined by fitting the integrated Balmer decrement, assuming recombination Case B at temperature $T_{\rm OIII}$. The values of $T_{\rm OIII}$, $n_{\rm opa}$ and $f_{\rm blend}^{HeI}$ are set by iteratively fitting $R_{\rm OIII}$ and the deblended [Ar IV] λ4711Å/λ4740Å ratio.

TABLE 2

OSALD PARAMETER FIT OF OBSERVED LINE RATIOS[a]

Objects		Target line ratios			Blending corrections			Parameter values		
(1) Index #	(2) AGN	(3) $H\alpha/H\beta$ $\frac{\lambda4861}{\lambda6563}$	(4) R_{OIII} $\frac{\lambda4363}{\lambda5007}$	(5) $[Ar\,IV]_+$ $\frac{\lambda4711+}{\lambda4740}$	(6) $R_{He/Ar}$ $\frac{\lambda5876}{\lambda4740}$	(7) f^{HeI}_{blend}	(8) [Ar IV] $\frac{\lambda4711}{\lambda4740}$	(9) τ_V^o	(10) n_{opa} cm^{-3}	(11)[b] T_{OIII} °K
1	Mrk 573	3.62	0.0119	1.156	2.03	0.044	1.108	0.16	1.56×10^3	12 760
2	Mrk 34	4.10	0.0110	1.193	2.46	0.047	1.140	0.41	1.85×10^3	12 660
3	Mrk 78	5.31	0.0075	1.238	4.05	0.062	1.166	1.10	2.48×10^3	11 510
4	Mrk 176	6.55	0.0139	1.045	0.90	0.013	1.031	1.74	6.54×10^3	15 210
5	Mrk 3	5.31	0.0141	0.850	3.00	0.068	0.796	1.08	1.37×10^4	14 560
6	Mrk 1	5.00	0.0136	0.814	2.71	0.067	0.762	0.91	1.40×10^4	14 150
7	NGC 1068	4.47	0.0129	0.763	3.56	0.106	0.690	0.61	1.49×10^4	13 500

[a]The line ratios were not corrected for reddening. A foreground dust screen was assumed instead whose opacity increases exponentially: $\tau_{ij} = \tau_V^o \exp(n/n_{opa})\, A(\lambda_{ij})/A_V$, where $A(\lambda_{ij})/A_V$ represents the extinction curve evaluated at wavelength λ_{ij} for the emission line ij considered.

[b]The averaged temperature for the sample is $\langle T_{OIII} \rangle = 13\,480 \pm 1180$ °K.

5.1.3. *Transposition to a Simplified Spherical Geometry*

The algorithm consists in integrating the line emission measures[17] of an isothermal multi-density plasma (MDP) of temperature T_e. The calculations can be transposed to the idealized geometry of a spherical (or conical) distribution of ionization bounded clouds whose densities n decrease as r^{-2}. The weight attributed to each plasma density component is set proportional to the *covering solid angle*[18] $\Omega(n)$ subtended by the plasma shell of density n. In the case of photoionization models, such a distribution would result in a constant ionization parameter U_o and the integrated columns N_{X_k} of each ion k of any cloud would be to a first order constant. For the sake of simplicity, to describe $\Omega(n)$ we adopt the power law $(n/n_{low})^{\epsilon}$, which extends from $n_{low} = 100$ up to $10^8\,cm^{-3}$. If we transpose this to a spherical geometry where both U_o and Ω are constant (i.e. $\epsilon = 0$), the *area* covered by ionization-bounded emission clouds would increase as r^2, thereby compensating the dilution of the ionizing flux and the density fall-out (both $\propto r^{-2}$). In this case, the weight attributed by OSALD to each shell is the same; otherwise, when $\epsilon \neq 0$ the weight is simply proportional to $\Omega(n)$. MDP calculations are not a substitute to photoionization calculations. They are only intended as diagnostics that could constrain some of the many free parameters that characterize multidimensional NLR models, including those which might consider a non-uniform dust distribution.

[17]Defined as the line emission coefficient times the electronic density.

[18]$\Omega(n) = A(n)/4\pi r^2$ where A is the area of a shell of density n exposed to the ionizing source at a distance r. For definiteness we set the electron density equal to that of H, $n = n_e = n_H$.

5.1.4. *Selection of the Distribution Index ϵ*

To guide us in the selection of ϵ, we followed the work of Be06b who determined that, for a spectral slit radially positioned along the emission line cone, the surface brightness of the *spatially resolved* ENLR is seen decreasing radially along the slit as r^{δ} (with $\delta < 0$), where r is the projected nuclear distance on the sky. From their [O III] λ5007Å and Hα line observations of Seyfert 2's, Be06b derived average index values of $\delta_{[OIII]} = -2.24 \pm 0.2$ and $\delta_{H\alpha} = -2.16 \pm 0.2$, respectively. Let us assume that such a gradient extends inward, i.e. inside the unresolved NLR. For our assumed spherical geometry where the Hα luminosity across concentric circular apertures behaves as $r^{-2\epsilon}$ (see § C.2), ϵ is given by $-(1+\delta)/2$. Hence we adopt $\epsilon \approx +0.6$ so that a long slit projected onto our spherical geometry could reproduce the observed $\delta_{[OIII]}$ value of Be06b. Out of curiosity, we have explored other positive values and found that changes in ϵ were not critical and did not affect our conclusions.

5.1.5. *Importance of Deblending the [Ar IV]$_+$ λ4711Å$_+$ Lines*

As emphasized by Kewley et al. (2019), care must be taken when interpreting the [Ar IV] doublet since

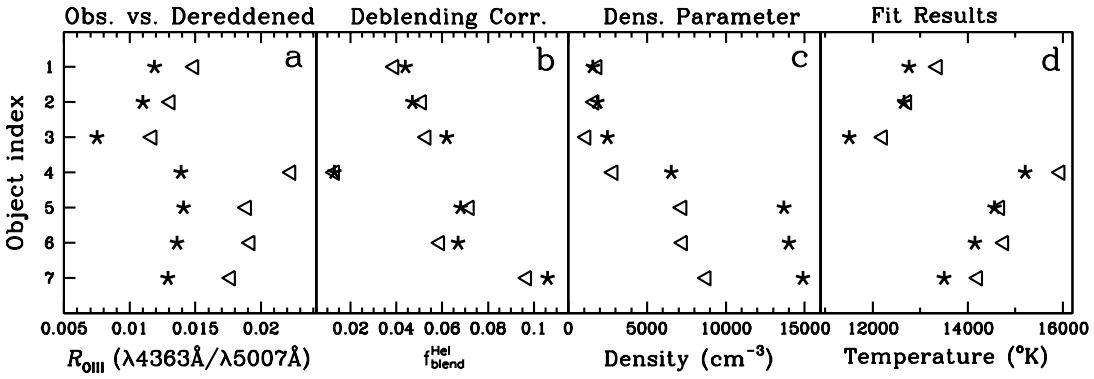

Fig. 4. Comparison between parameters and plasma temperatures shown in Table 1 (open triangles) and Table 2 (stars). An index number (1 – 7) identifies the object name in Column (2) of either table. Panel a: target $R_{\rm OIII}$ ratios, dereddened (open triangles) vs. observed (stars). Panel b: deblending corrections $f^{HeI}_{\rm blend}$ applied to the [Ne IV] doublet ratios. Panel c: sharp density cut-off (open triangles) vs. extinction density cut-off $n_{\rm opa}$ (stars). Panel d: plasma temperatures inferred from the dustfree model (open triangles) vs. dusty screen model (stars).

the weak nearby He I λ4713Å line is nearly superposed to the [Ar IV] λ4711Å line, hence the need to apply a proper deblending correction to the measured [Ar IV] ratios. The procedure adopted is described in Appendix B.1. Because of the relative weakness of the He I λ4713Å line, there is no direct evidence of its presence in AGN spectra given its closeness to the [Ar IV] λ4711Å line. To deblend the flux contribution from the He I λ4713Å line, we first evaluate its expected flux using the strong He I λ5876Å line and then subtract it from the [Ar IV] λ4711Å line. Since we are dealing with He recombinations lines, the dependence of the He I ratio on temperature or density is relatively minor. Hence, obtaining a reliable estimate of the He I fractional contribution, $f^{HeI}_{\rm blend}$, to the observed [Ar IV] profile is straightforward. The procedure is described in Appendices B.1 and C.4.

Another potential blending consists of the first two lines of the [Ne IV] quadruplet which comprise the lines λ4714.36, λ4715.80, λ4724.15 and λ4726.62Å (García-Rojas et al. 2015). For convenience, we will refer to them as consisting of two doublets centered at λλ4715Å and λλ4725Å, respectively. Up to densities of $\approx 10^6\,{\rm cm}^{-3}$, the unblended λλ4725Å doublet is calculated to be on average 35% brighter than the λλ4715Å doublet. In those cases where the λλ4725Å doublet is detected, we can reliably determine the blended λλ4715Å doublet flux and then subtract it from the blended [Ar IV]$_+$ λ4711Å$_+$ lines. Further information about the deblending procedure is given in Appendix B.2. No detection of the [Ne IV] λλ4725Å line was reported by Kos78.

5.2. *Results from the Multi-Density Plasma Models*

5.2.1. *The Reference Seyfert 2 Sample*

The results from the calculations using OSALD are presented in Table 2, where we have assumed a power law index of $\epsilon = +0.6$. In Column (7), $f^{HeI}_{\rm blend}$ represents the estimated blending contribution from He I λ4713Å to the [Ar IV]$_+$ λ4711Å$_+$ lines. The resulting deblended [Ar IV] λ4711Å/λ4740Å ratios are presented in Column (8). The foreground dust screen opacities, τ^o_V, inferred by OSALD from the observed Balmer decrements (Column 3) are given in Column (9). The fitted dust distribution e-folding densities, $n_{\rm opa}$, and the inferred plasma temperatures are given in Columns (10) and (11), respectively.

To facilitate the evaluation of these fits, we show in Figure 4 how the parameters compare for each object between Table 1 (triangles) and Table 2 (stars). Panel (a) represents the target $R_{\rm OIII}$ ratios, dereddened vs. observed, Panel (b) the deblending correction $f^{HeI}_{\rm blend}$, Panel (c) the the cut-off density vs. dust drop-out density scale, and Panel (d) the temperatures inferred from the fits. The e-folding dust screen densities, $n_{\rm opa}$, derived by OSALD lie in the range 1500 to 16 000 cm^{-3}. The average $\langle {\rm T_{OIII}} \rangle$ for the seven Seyfert 2's is $13\,480 \pm 1180$ °K, being lower by only 500 °K with respect to the single density case.

Having considered an explicit density distribution, with either dust obscuration (Column 10) or without (see Table B1 in Appendix E), we derive temperature values that do not differ much from the single density case of Table 1. This supports our contention that collisional deexcitation is not affecting significantly the $R_{\rm OIII}$ ratios observed by

TABLE 3

EXPLORATION WITH OSALD OF BLENDING DUE TO [Ne IV] λλ4714,16Å

Objects		Target line ratios			Dual blending corrections[a]					Parameter values		
(1) Index #	(2) AGN	(3) $\frac{H\alpha}{H\beta}$ $\frac{\lambda4861}{\lambda6563}$	(4) R_{OIII} $\frac{\lambda4363}{\lambda5007}$	(5) $[Ar\,IV]_+$ $\frac{\lambda4711+}{\lambda4740}$	(6) $R_{He/Ar}$ $\frac{\lambda5876}{\lambda4740}$	(7) f^{HeI}_{blend}	(8) $R_{Ne/Ar}$ $\frac{\lambda4725}{\lambda4740}$	(9) f^{NeIV}_{blend}	(10) [Ar IV] $\frac{\lambda4711}{\lambda4740}$	(11) τ^o_V	(12) n_{opa} cm^{-3}	(13) T_{OIII} °K
1	Mrk 573	3.62	0.0119	1.156	2.03	0.053	0.30[b]	0.203	0.921	0.15	3.59×10^3	12 710
2	Mrk 34	4.10	0.0110	1.193	2.46	0.056	0.30[b]	0.196	0.953	0.40	4.56×10^3	12 610
3	Mrk 78	5.31	0.0075	1.238	4.05	0.075	0.30[b]	0.190	0.979	1.09	6.45×10^3	11 470
4	Mrk 176	6.55	0.0139	1.045	0.90	0.017	0.30[b]	0.220	0.845	1.73	1.47×10^4	15 120
5	Mrk 3	5.31	0.0141	0.850	3.00	0.089	0.30[b]	0.307	0.609	1.08	2.76×10^4	14 390
6	Mrk 1	5.00	0.0136	0.814	2.71	0.089	0.30[b]	0.326	0.575	0.91	2.85×10^4	13 950
7	NGC 1068	4.47	0.0129	0.763	3.56	0.146	0.30[b]	0.373	0.502	0.61	3.11×10^4	13 250
8A	NGC 4151[c]	5.29	0.0222	0.727	2.40	0.064	–	–	0.684	1.07	2.16×10^4	18 050
8B	" "	"	"	"	"	0.088	0.30[d]	0.377	0.496	1.07	4.64×10^4	17 610
8C	" "	"	"	"	"	0.148	0.62[e]	1.32	0.294	1.08	1.49×10^5	16 180
9	Mrk 477	4.00	0.0215	0.693	7.05	0.295	0.30	0.35	0.535	0.34	22 200	16 350
10	J1653+23[f]	4.08	0.0192	1.16	4.76	0.099	0.42	0.25	1.05	0.39	2 840	16 050
11	J1300+53	3.79	0.0257	1.13	3.21	0.070	0.38	0.22	1.06	0.239	2 200	18 320

[a]The fraction of $[Ar\,IV]_+$ contributed by blending is the sum of $f^{HeI}_{blend} + f^{NeIV}_{blend}$.

[b]The quoted [Ne IV] doublet ratio of 0.30 is our estimated upper limit for the Kos78 sample.

[c]The line ratios measurements of the Seyfert I NGC 4151, are from Boksenberg et al. (1975).

[d]Eye estimate of the [Ne IV] λ4725Å doublet from the Boksenberg et al. (1975) spectrum.

[e]Value of the [Ne IV] λ4725Å doublet deduced from Table I of Boksenberg et al. (1975).

[f]Observations carried out with the spectrograph OSIRIS mounted on the 10.4 m Gran Telescopio Canarias.

Kos78. Given the relative proximity in Figure 3 of the Ri14 subset a41 (black diamond) to the Kos78 sample (black disk), we might conjecture that LDR possibly applies to the a41 sample as well since, at a redshift of $z = 0.11$, the large projected scale of the $3\widehat{''}$ SDSS aperture ensures significantly more dilution of the inner dense NLR component in comparison to the Be06b and Kos78 samples. We would need a larger sample of [Ar IV] doublet measurements to confirm that R_{OIII} translates into a reliable determination of the plasma temperature in Type II AGN.

5.2.2. *Probing the Possible Blending of [Ar IV] by [Ne IV]*

We present complementary calculations in Table 3 where we have assumed the hypothetical case of the λλ4725Å doublet reaching 30% of the observed [Ar IV] λ4740Å line intensity. The blending contributions from the He I and [Ne IV] λλ4715Å lines, that is f^{HeI}_{blend} and f^{NeIV}_{blend}, are presented in Columns (7) and (9), respectively, and the resulting deblended [Ar IV] doublet ratios are listed in Column (10). The opacities τ^o_V (Column 11) inferred remain about the same, but the e-folding densities n_{opa} (Column 12) are typically larger with respect to Table 2. The average sample temperature $\langle T_{OIII} \rangle$ is lower by only 125 °K. At least for the Kos78 sample at hand, not including the λλ4725Å doublet should not affect our conclusions concerning the Seyfert 2 NLR temperatures.

5.2.3. *Detection of [Ne IV] in Nearby Seyfert 1 NGC 4151*

The critical densities of the [Ne IV] quadruplet lines all lie above $10^6\,cm^{-3}$. Because the [Ar IV] doublet emissivities at such densities are significantly reduced due to collisional deexcitation, a positive detection of the [Ne IV] λλ4725Å doublet might relate to having plasma densities much above those deduced from the Kos78 sample. This might be the case in Type I AGN. Interestingly, the detection of the [Ne IV] λλ4725Å doublet was reported early on in the Seyfert 1 NGC 4151 by Boksenberg et al. (1975). The line ratios of interest for this object are shown

in Table 3. A labeled star depicts its position in Figure 3. Eye estimates of the [Ne IV] $\lambda\lambda$4725Å doublet (from the published figure) suggest a value of ≈ 0.3 with respect to the [Ar IV] λ4740Å line, while the measurements reported in their Table I would imply a higher value of 0.62. In Table 3, we present three OSALD fits in which the [Ne IV]/[Ar IV] ratio (Column 8) successively takes on the values of 0, 0.3 and 0.62. The two [Ne IV] deblending corrections result in $n_{\rm opa}$ values higher by factors of 2.2 and 7.5 for models 8B and 8C, respectively, with the deblended [Ar IV] doublet ratios dropping to 0.496 and 0.294 (Column 10). The impact on the inferred temperature is significant, with T_{OIII} from model 8C being 1870 °K lower, at 16 180 °K, showing minimal evidence of collisional deexcitation being present. It would be interesting to repeat this exercise if we could obtain higher S/N spectra.

5.2.4. *The Particular Case of QSO 2's*

Through our literature search of Type II AGN measurements of the $\lambda\lambda$4725Å [Ne IV] doublet, we came across three objects classified as QSO 2's, that is, Type II quasars corresponding to the high luminosity counterpart of Seyfert 2's. They are Mrk 477 (Villar Martín et al. 2015), SDSS J1300+54 and SDSS J1653+23 (Villar-Martín et al. 2017) at redshifts z of 0.037, 0.088 and 0.103, respectively. Their spectra were extracted from the Sloan Digital Sky Survey data (SDSS; York et al. 2000) and the line ratios relevant to our analysis are given in Table 3.

What stands out from these objects is their larger $R_{\rm OIII}$ ratios. The deblended [Ar IV] doublet ratios (Column 8) do not imply significant collisional deexcitation, except at a reduced level in Mrk 477 where $n_{\rm opa}$ reaches $\simeq 22\,200\,{\rm cm}^{-3}$. Yet the T_{OIII} values inferred (Column 13) for the three QSO 2's are much higher than in Seyfert 2's, which questions the plausibility of LDR conditions. It is possible that AGN's where the [Ne IV] $\lambda\lambda$4725Å can be detected might indicate the presence of a double-bump in their density distribution. We tentatively explored the addition of an additional denser plasma component ($\gtrsim 10^6\,{\rm cm}^{-3}$) to our power law. Our fit to the [Ar IV] doublet was not very sensitive to this component since both $\lambda\lambda$4711,40Å lines are affected by collisional deexcitation at the high density end. Even though the temperatures we inferred came out at values lower than in Column (13), the exercise was not convincing as the number of free parameters exceeded the number of variables. A possible interpretation is that the super-luminous QSO 2's scale up in size to the extent that their inner NLR become partly visible, as is the case of the high spatial resolution HST measurement of the nearby Seyfert 2 NGC 1068 (c.f. red triangles in Figure 1).

6. TEMPERATURE PROBLEM WITH PHOTOIONIZATION

In conclusion, after integrating the emissivities of the [O III] and [Ar IV] lines over a continuous distribution of densities, we find that the impact of collisional deexcitation on the λ4363Å/λ5007Å ($R_{\rm OIII}$) ratio is not significant among ground-based observations of the seven Seyfert 2 sample of Kos78 who provided measurements of the [Ar IV] density indicator and, therefore, their $R_{\rm OIII}$ ratio provides us with a reliable measurement of the NLR temperature. A comparison of the values of $R_{\rm OIII}$ observed among quasars, Seyfert 2's and spatially extended ENLR plasma, as displayed in Figure 1, argues in favor of a floor temperature for the NLR, which we situate at $\gtrsim 13\,500$ °K. Our photoionization models using MAPPINGS Ig and assuming standard SEDs and low densities predict $R_{\rm OIII}$ values significantly below those observed in Seyfert 2's. This discrepancy defines what we would label the $R_{\rm OIII}$-temperature problem.

In the current work, we found complementary evidence that the orientation of the emission line cone with respect to the observer's line-of-sight affects our characterisation of the NLR, whether in Seyfert 2's (Kos78 sample) or in quasars (BL05 and RA00 samples). We do not exclude the existence of a much denser NLR component being present in ground-based observations, but we would propose that, at least among Seyfert 2's with $z \gtrsim 0.02$, the latter would be strongly diluted by the much brighter low density NLR component, which we evaluate to have a density $\lesssim 10^{4.3}\,{\rm cm}^{-3}$. In quasars, where a larger fraction of this dense and luminous component becomes visible, the resulting $R_{\rm OIII}$ ratio progressively increases up to values of ≈ 0.2 due to collisional deexcitation, as proposed by BL05 using dual-density photoionization models. It would be interesting to investigate whether the [Ne IV] λ4725Å doublet becomes intrinsically stronger in Type I objects. A few luminous AGN in which we reported the detection of the [Ne IV] doublet in § 5.2.3 and 5.2.4 appear to favor a density distribution akin to a double-bump, such as the dual-density approach of BL05, rather than the single power law we have assumed.

This work has been partly funded with support from the Spanish Ministerio de Economía y

Competitividad through the grant AYA2012-32295. G.MC is grateful for the support from the Centro de Investigaciones de Astronomía (CIDA). A.R.A acknowledges partial support from CNPq Fellowship (312036/2019-1 and 203746/2017-1). M.M-P acknowledges support by the Korea Astronomy and Space Science Institute for her postdoctoral fellowships. A. Alarie was funded by a postdoctoral grant from CONACyT. We thank the referee for his/her helpful constructive comments.

The discussion about the referred three QSO 2's is based on data from the Sloan Digital Sky Survey. Funding for the SDSS and SDSS-II has been provided by the Alfred P. Sloan Foundation, the Participating Institutions, the National Science Foundation, the US Department of Energy, the National Aeronautics and Space Administration, the Japanese Monbukagakusho, the Max Planck Society and the Higher Education Funding Council for England. The SDSS website is http://www.sdss.org/. The SDSS is managed by the Astrophysical Research Consortium for the Participating Institutions.

APPENDICES

A. THE VALIDITY OF LOW DENSITY REGIME FOR THE ENLR

Among the Seyfert galaxies studied (e.g. Bennert et al. 2006a,b), the ENLR densities inferred from the red [S II] $\lambda\lambda$6716,31Å doublet are typically $< 10^3\,\mathrm{cm}^{-3}$. Along the long-slit measurements, in most cases both the electron density and the ionisation parameter appear to be decreasing with radius. The authors proposed that deviations from this general behaviour (such as a secondary peak), when seen in both the ionisation parameter and electron density space, can be interpreted as signs of shocks due to the interaction with a radio jet. In what follows, we will consider those cases where the excitation mechanism is photoionization by the accretion disk. The red dot in Figure 1 represents the average R_{OIII} of the ENLR of four[19] Seyfert 2's observed by SB96. If we assume a temperature of 9 000 °K for the [S II] plasma, the densities inferred by BWS from the λ6716Å/λ6731Å ratios from each ENLR are $\leq 250\,\mathrm{cm}^{-2}$. Two other examples shown in Figure 1 are: (a) the yellow filled dot, which corresponds to a deep spectrum of a 8 kpc distant cloud from the nucleus of radio-galaxy Pks 2152-699 (Ta87), and (b) the magenta dot which represents the average R_{OIII} of seven optical filaments situated at ≈ 490 pc from the nucleus of the radio-galaxy Centaurus A (Mo91). In both cases, the red [S II] doublet measurements indicate low electronic densities, with $n_e \leq 250\,\mathrm{cm}^{-3}$.

High excitation ENLR lines such as [O III] should similarly operate under LDR conditions for the following reasons. First, the geometrical dilution factor of the ionizing flux across the typical detector aperture does not vary significantly. For instance, if we define r_{in} as the radial distance separating the UV source from the inner boundary of the observed ENLR, and Δr as the radial thickness corresponding to the detector aperture projected on the sky, then the ratio $(\Delta r/r_{in})^2$ represents the fractional change of the UV dilution factor across the observed ENLR. This factor is typically $\lesssim 1.5$, indicating that the observed plasma is exposed essentially to the same ionizing flux. Line ratio variations across Δr must be due to either variations in plasma density or to a progressive absorption of the ionizing radiation, but not to changes in the dilution factor. Second, if the [O III] and [S II] lines originate from unrelated gas components, the densities of the low [S II] emission plasma must be orders of magnitudes *higher* than the [O III] emission plasma in order to sufficiently reduce the ionization parameter to the point that the low ionization species dominate the spectrum. Third, if the [S II] emission corresponds to the partially ionized layer at the back of a photoionized (ionization-bounded) slab, the electronic density of the region that emits the [O III] lines is denser by a factor of 2.5 to 4. The reason is that the [S II] emission comes from plasma that is partially ionized with an electronic density n_e much lower than the local gas density n_H. This factor is sufficiently small that for the typical [S II] densities of $n_e \simeq 250\,\mathrm{cm}^{-3}$ as found in the ENLR, the density associated to the [O III] lines would still be $\ll 10^4\,\mathrm{cm}^{-3}$ and LDR conditions should therefore apply.

B. CORRECTING THE [Ar IV] DOUBLET FOR LINE BLENDING

B.1. *Correcting the [Ar IV]$_+$ Ratio for He I λ4713Å Blending*

One characteristic of ratios involving recombination lines of the same ion is their limited sensitivity to either temperature or density. A satisfactory prediction of the He I λ4713Å line intensity can be derived from the measurement of the He I λ5876Å line. First, we derive the Case B He I λ4713Å/λ5876Å ratio, which we label $\mathrm{R_{He}}$, via interpolation of the emissivities from the supplemental

[19] Each of these measurements is associated to a Seyfert 2 as we left out the fifth object, NGC 526A, which is classified as Seyfert 1.5.

table of Porter et al. (2013). For a $10^4\,cm^{-3}$ plasma at a temperature of 12 000 K, R_{He} turns out to be only 4.78% of He I 5876Å. Temperature variations of ±2000 °K would cause a change in this ratio of $^{+7.95}_{-11.5}$%, respectively, while adopting density values of 100 and $10^5\,cm^{-3}$ would result in R_{He} ratios of 0.0429 and 0.0489, respectively. Second, by defining $R_{He/Ar}$ as the observed He I/[Ar IV] λ5876Å/λ4740Å ratio, the product $(R_{He/Ar} \times R_{He})$ defines our estimate of the blending contribution from He I λ4713Å to the *measured* (blended) [Ar IV]$_+$ doublet ratio. The relevant information is provided by the fractional contribution of the blended line, which is given by $f^{HeI}_{blend} = (R_{He/Ar} \times R_{He})/[Ar\,IV]_+$. The blended-corrected [Ar IV] λ4711Å/λ4740Å doublet ratio is given by $(1 - f^{HeI}_{blend}) \times [Ar\,IV]_+$, which was used to explore the single density case discussed in § 4.2 (see Column (7) of Table 1). For the power law density distribution case, the procedure is described in § C.4.

B.2. *Correcting the [Ar IV]$_+$ ratio for [Ne IV] λλ4715Å Blending*

The [Ne IV] optical lines consist of a quadruplet at λ4714.36, λ4715.80, λ4724.15 and λ4726.62Å, respectively (García-Rojas et al. 2015). To simplify the notation, we will refer to the quadruplet as consisting of two doublets: the observed [Ne IV] λλ4725Å lines and the potentially blended [Ne IV] λλ4715Å lines. At typical NLR densities, the potentially observed [Ne IV] λλ4725Å doublet is calculated to be ≈ 35% brighter than the [Ne IV] λλ4715Å doublet (blended with [Ar IV] λ4711Å). To our knowledge the [Ne IV] λλ4725Å doublet has only been reported in a few AGN. However, it is frequently observed in planetary nebulae (PN). For instance, in NGC 6302, where the stellar temperature is estimated to be in the range 224 000 to 450 000 °K (Feibelman 2001), the observed [Ne IV]/[Ar IV] λλ4725Å/λ4740Å ratio reported by Aller et al. (1981) is 0.175. Since the emission lines of PN are narrow, the above mentioned lines can be resolved without any need of deblending provided high resolution spectroscopy has been carried out. For instance, the observations of the PN NGC 3918 by García-Rojas et al. (2015) using the Ultraviolet-Visual Echelle Spectrograph (UVES, D'Odorico et al. (2000)) with a $1\overset{\frown}{''}$ slit resulted in a spectral resolution of 6.5 km s^{-1}. The observed emission profiles of each [Ne IV] quadruplet line were well resolved, showing a FWHM of ≃ 20 km s^{-1}. Interestingly, the [Ne IV]/[Ar IV] λλ4715Å/λ4711Å and He I/[Ar IV] λ4713Å/λ4711Å ratios measured by García-Rojas et al. (2015) are 0.115 and 0.078, respectively. To correct the measured [Ar IV]$_+$ (λ4711Å$_+$/λ4740Å) ratio for [Ne IV] blending, the density integration by OSALD of the two doublets [Ne IV] λλ4724,26Å and [Ne IV] λλ4714,16Å proceeds as described in Appendix C.4 for the He I λ4713Å and λ5876Å lines.

C. THE OSALD ALGORITHM

Using emission line atomic physics, OSALD[20] explores temperature and density diagnostics in which an explicit distribution of the density is considered.

C.1. *Line Diagnostics with a Power Law Density Distribution*

Our goal is to explore which density distribution best reproduces a given set of line ratios, and to determine to what extent collisional deexcitation is affecting the observed R_{OIII} λ4363Å/λ5007Å or R_{NII} λ5755Å/λ6583Å line ratios. For the high ionization species such as O^{+2}, Ar^{+3} and Ne^{+3}, the temperature T_{OIII} is set iteratively to the value which reproduces the target R_{OIII} ratio. Although not considered in the current paper, other diagnostics can be modeled, such as the singly ionized oxygen [O II] λ6726Å/λ6729Å and [O II] λ3727Å/λ7325Å line ratios at the temperature that would reproduce the temperature sensitive R_{NII} target ratio, or the singly ionized sulphur [S II] λ6716Å/λ6731Å and [S II] λλ4069,76Å/λλ6716,31Å line ratios at the estimated temperature $T_{SII} \approx 9000$ °K.

C.2. *Transposition of OSALD to a Spherical Geometry*

The isothermal plasma considered by OSALD can be visualized as consisting of concentric shells of plasma whose densities decrease radially as r^{-2}. These shells are given a weight which we associate to the covering solid angle of a putative ionizing source at the center. This can be transposed to the idealized case of photoionized shells that are ionization bounded and share the same ionization parameter U_o. To the extent that the low density regime applies, the line luminosities of each shell result equal if they share the same covering *solid angle* Ω of the ionizing source. OSALD basically integrates the line emission coefficient times the shell covering solid angle: $j^k_{ij}(n,T)\,\Omega(n)\,\Delta n$, where ij corresponds to the transition from levels j to i evaluated at a temperature T and a density n, which takes into account collisional deexcitation. The integrated line flux for line

[20] Stands for "Oxygen Sulfur Argon Line Diagnostic".

ij of ion k reduces to the summation in density space of $\sum_l \Omega(n_l)\ j_{ij}^k(T, n_l)\ \Delta n_l$, where n_l is progressively increased in locked steps of size $\Delta n_l/n_l = 0.004$ dex from $n_H^o = 100$ up to the cut-off density $n_{\rm cut}$. When the fit incorporates foreground dust extinction, $n_{\rm cut}$ is fixed at $10^8\,{\rm cm}^{-3}$ and the actual cut-off is set by the foreground dust extinction which increases exponentially with density. The e-folding density for the opacity in the V-band is defined by the parameter $n_{\rm opa}$(see C.3). The weight of each shell is given by its covering solid angle Ω, which follows a power law of index ϵ with density: $\Omega(n) = \Omega_o\ (n/n_H^o)^\epsilon$, where Ω_o is an arbitrarily small constant that would ensure negligible shell shadowing. The density is postulated to decrease radially as $n \propto r^{-2}$. As a result, the shells' luminosities behave as $r^{-2\epsilon}$ since positive values of ϵ imply a covering solid angle that increases towards the ionizing source (along with the density n). A slit radially positioned along the ionizing cone would result in an Hβ surface brightness that decreases as r^δ, with $\delta = -(2\epsilon + 1)$.

C.3. *Line Transfer Across the Cone-Like Dust Screen*

In the context of Type II objects, we propose in § 5 that each emission line is seen through a dust screen whose opacity increases exponentially towards the inner denser regions. For each line ij, the opacity $\tau_{ij}(n)$ is given by $\tau_V^o \exp(n/n_{\rm opa})\, A(\lambda_{ij})/A_V$, where τ_V^o is the V-band dust opacity at the lowest density n_H^o, $n_{\rm opa}$ is the e-folding density of the exponential function, $A(\lambda_{ij})$ the selected extinction curve and A_V the extinction value at 5 500Å. When integrating the emission measures, the dust transfer function ${\rm Tr}(\tau_{ij}(n))$ is applied to each emission coefficient $j_{ij}^k(n, T)$. The latter assumes a plane-parallel geometry and takes into account both absorption and scattering due to the dust grains, as described in Appendix C of Binette et al. (1993). In order to constrain the parameter τ_V^o, the set of line ratios that are selected to be fitted must include one or more Balmer line ratios from H.

C.4. *Blending of the He I λ4713Å and [Ar IV] λ4711Å Lines*

To calculate the flux of any He I line, the Case B recombination coefficients are taken from the work of Porter et al. (2013). They cover the temperature range $5\,000 \le T_{rec} \le 25\,000$ °K and density range $10^2 \le n_e \le 10^{14}\,{\rm cm}^{-3}$. By default, the temperature assumed for He I in the current work is $T_{rec} = 12\,000$ °K while it is the variable $T_{\rm OIII}$ for [Ar IV] and all the high ionization ions.

In order to evaluate the blending of the weak He I λ4713Å line with the [Ar IV] λ4711Å line, OSALD integrates the emission flux of the following four lines: He I λ4713Å, He I λ5876Å, [Ar IV] λ4711Å and [Ar IV] λ4740Å, taking into account dust extinction at the corresponding densities. This procedure properly takes into account how the emission coefficient of each line is affected by density and collisional deexcitation, as well as by dust extinction, which may increase along with density. After assuming an arbitrary abundance ratio of the two ionic species He^+ and Ar^{+3}, the algorithm derives the integrated He I/[Ar IV] ratio labelled $R_{5876/4740}$ and rescales it to the observed value. The $R_{4713/4740}$ ratio represents a measure of the blending contribution from He I and is derived from the ratio $R_{4713/5876}/R_{5876/4740}$. Deblending the [Ar IV] $R_{4711/4740}$ ratio is achieved by subtracting the $R_{4713/4740}$ ratio from the observed blended $[{\rm Ar\,IV}]_+$ ratio. The fraction of $[{\rm Ar\,IV}]_+$ due to He I blending is labelled $f_{\rm blend}^{HeI}$ in all our tables.

C.5. *Minimum $\chi^2_{\rm rno}$ and Iterative Least Squares Fit*

We used a non-linear least squares fit method to find the optimal input parameter values that succeed in reproducing as closely as possible the target line ratios. These parameters are varied in an iterative fashion until the minimum re-normalized $\chi^2_{\rm rno}$ value is encountered, with $\chi^2_{\rm rno}$ defined as

$$\chi^2_{\rm rno}(x_j) = \sum_{i=1}^{m} \frac{w_i \left(y_i - y(x_j)\right)^2}{MAX\left[y_i^2\,,\, y(x_j)^2\right]} \Big/ \sum_{i=1}^{m} w_i, \quad \text{(C1)}$$

where m is the number of line ratios simultaneously fitted, w_i the weight attributed to each line ratio i, y_i the observed target line ratios and $y(x_j)$ the corresponding line ratios derived from the integration of the line fluxes. The quantity x_j represents the various parameters on which the line integration depends, that is, the temperature T_{fit} and density n, as well as the parameters describing the behaviour of the covering angle $\Omega(n)$, which are ϵ and $n_{\rm cut}$ as defined in Appendix C.2. As detailed in § 5.2 and Table 2, we used the algorithm to fit the line ratios of the seven Type II NLR of Table 1. By trial and error we settled for weights w_i of 2.0 and 1.5 for the [Ar IV] λ4711Å/λ4740Å and $R_{\rm OIII}$ λ4363Å/λ5007Å ratios, respectively.

OSALD's basic goal is to evaluate whether or not there is evidence of significant collisional deexcitation affecting the $R_{\rm OIII}$ ratio of any AGN whose

λ4711Å/λ4740Å ratio is successfully measured. Any fit where $\chi^2_{\rm rno}$ exceeds 0.05 is deemed unsatisfactory and of no use. The fits described in Tables 1–3 all present a negligible $\chi^2_{\rm rno} \approx 5 \times 10^{-7}$. For this reason, the line ratios derived from the fits are, for all practical purposes, equal to the target ratios.

D. NLR ORIENTATION AND THE OBSERVER'S PERSPECTIVE

The geometrical set-up behind the *unified model* may apply not only to the BLR but to parts of the NLR that are gradually obscured in Type II objects. This would explain why the NLR line emission observed in the Seyfert 2's correspond to a much lower density plasma than observed in Type I's. Examples of studies confirming the impact of the observer's perspective on the NLR are:

(a) Using a data set of 18 Seyfert 1 and 17 Seyfert 2 of similar redshift from the literature, Murayama & Taniguchi (1998) showed the evidence of an excess of Fe VII λ6086Å emission in Type I AGN with respect to Type II. The Fe VII/[O III] (λ6087Å/λ5007Å) ratio in Type I AGN turns out to be an order of magnitude larger than in Type II. They proposed that it was linked to a region residing in the inner wall of a dusty torus, which they labeled the high-ionization nuclear emission line region (HINER[21]).

(b) Using a sample of 214 Seyferts, Nagao et al. (2001, hereafter NMT) confirmed that Type I Seyferts show a statistically higher $R_{\rm OIII}$ than Type II Seyferts. Using the work of De Robertis & Osterbrock (1984, 1986) who measured the line widths of 24 Seyferts, MNT found that the FWHM of [O III] λ4363Å in Type I spectra was larger than that of [O III] λ5007Å , while in Type II spectra the FWHM of both lines were statistically indistinguishable. Although with less statistical significance, two more results were presented by NMT: (1) the FWHM of [O III] λ4363Å was larger in Type I than in Type II spectra, and (2) the FWHM of [O III] λ5007Å in Type I and Type II spectra were statistically indistinguishable. The authors commented that these results suggest that the strongly [O III] λ4363Å emitting region is located in a deeper inner region as compared to [O III] λ5007Å and that it is fully visible only in Type I AGN. MNT inferred that the dependence of $R_{\rm OIII}$ on AGN types could be attributed to obscuration effects.

(c) Meléndez et al. (2008) favour a similar interpretation with respect to the mid-infrared coronal lines. They found that the mean [O III] λ5007Å line luminosity is 1.4 dex smaller in Seyfert 2's than in Seyfert 1's, while in the case of the mean [O IV] λ25.89 μm line luminosity the difference between the two subgroups is only 0.2 dex. Their linear regression in the log plane of each AGN subgroup reveals that the luminosity of [O III] scales almost linearly as $L^{0.9\pm0.1}_{[O\,IV]}$ in Seyfert 1's, but much more steeply, as $L^{1.8\pm0.5}_{[O\,IV]}$ in Seyfert 2's. Both trends are consistent with strong dust absorption of [O III] while [O IV] is relatively little affected by extinction. It confirms earlier reports of Jackson & Browne (1991); Cameron et al. (1993); Mulchaey et al. (1994); Keel et al. (1994); Rhee & Larkin (2005); Netzer et al. (2006) that a much higher dust extinction affects the optical NLR of Seyfert 2's than of Seyfert 1.

(d) Finally, the work of Rose et al. (2015b,a) of Coronal-Line Forest Active Galactic Nuclei (CLiF AGN), which are characterized by a rich spectrum of optical forbidden high-ionization lines, suggests that the inner obscuring torus wall is the most likely location of the coronal line region.

[21] Terminology suggested by Murayama et al. (1998) to contrast those AGN from LINER.

E. DUST-FREE OSALD CALCULATIONS

In § 4.2, we assumed a single plasma density to determine the plasma temperature of the Kos78 Seyfert 2 sample. We present in Table B1 calculations from OSALD where the density is represented by a power law density distribution of index $\epsilon = +0.6$ that extends from $n = 100\,{\rm cm}^{-3}$ up to a sharp cut-off density $n_{\rm cut}$. The blending corrected [Ar IV] λ4711Å/λ4740Å ratios are given in Column (4) where we followed the procedure described in Appendices B.1 and C.4 to evaluate the He I λ4713Å fractional contribution $f^{HeI}_{\rm blend}$ to the blended [Ar IV]$_+$ line. The free parameters $n_{\rm cut}$ and $T_{\rm OIII}$ were iteratively varied until they reproduced the dereddened ratios of both $R_{\rm OIII}$ (Column 4) and (blended) [Ar IV]$_+$ (Column 5) from data Table 1. The inferred values for $n_{\rm cut}$ and $T_{\rm OIII}$ are given in Columns (5–6) of Table B1.

The plasma temperatures $T_{\rm OIII}$ of Table B1 are essentially the same as those of Column (9) from Table 1 that were derived assuming a single density.

TABLE B1

DUSTFREE FIT OF DEREDDENED RATIOS[a]

(1) Index	(2) Seyfert 2 Name	(3) $f^{HeI}_{\rm blend}$	(4)[b] [Ar IV] $\frac{\lambda4711}{\lambda4740}$	(5) $n_{\rm cut}$ cm^{-3}	(6)[c] $T_{\rm OIII}$ °K
1	Mrk 573	0.039	1.12	3.07×10^3	13 390
2	Mrk 34	0.051	1.15	2.73×10^3	12 720
3	Mrk 78	0.053	1.20	1.87×10^3	12 220
4	Mrk 176	0.013	1.03	4.78×10^3	15 930
5	Mrk 3	0.072	0.78	1.27×10^4	14 650
6	Mrk 1	0.059	0.78	1.27×10^4	14 740
7	NGC 1068	0.097	0.72	1.56×10^4	14 190

[a]Based on the reddening corrected line ratios of Table 1. The fits to both the $R_{\rm OIII}$ ratio and [Ar IV] doublet assume a density distribution that extends from 100 cm^{-3} up to the cut-off density $n_{\rm cut}$. The plasma covering factor follows a power law function of density with index $\epsilon = +0.6$.

[b]The target [Ar IV] λ4711Å/λ4740Å ratios after the He I deblending corrections have been applied to the observed values given in Column (5) of Table 1.

[c]The averaged temperature for the sample is $\langle T_{\rm OIII} \rangle$ = 13 380 °K.

The main reason is that, insofar as the [O III] lines are concerned, the line emissivities for the whole sample take place in the low density regime and, as a result, the density averaged over the whole distribution, $\bar{n}$, turns out to be very close to the single density value $n_{\rm sng}$ from Table 1 (Column 8). For instance, for the object with the highest cut-off density of Column (5), NGC 1068, the ratio $R_{\rm OIII}$ increases by only 3% across the range of densities covered by the power law distribution and the average density, $\bar{n}$, is 9425 cm^{-3}, which is close to the single density $n_{\rm sng}$ value of 8770 cm^{-3}. For the four objects where $n_{\rm cut} < 10^4$ cm^{-3}, the mean densities $\bar{n}$ are proportionally closer to the corresponding $n_{\rm sng}$ values.

We conclude that for a covering angle Ω that increases monotonically with density, there is no evidence of the $R_{\rm OIII}$ ratio being affected by collisional deexcitation among the Seyfert 2 sample of Kos78. We cannot rule out the existence of a double bump being present in the density distribution of some AGN. The cause could be the existence of a high density component above $\gtrsim 10^6$ cm^{-3} since such component would not contribute to the [Ar IV] lines and, therefore, our modelling would not be sensitive to it. There are indications that such a component might be present in QSO 2's, as proposed in § 5.2.4.

REFERENCES

Allen, J. T., Hewett, P. C., Richardson, C. T., Ferland, G. J., & Baldwin, J. A. 2013, MNRAS, 430, 3510, https://doi.org/10.1093/mnras/stt151

Aller, L. H., Ross, J. E., O'Mara, B. J., & Keyes, C. D. 1981, MNRAS, 197, 95, https://doi.org/10.1093/mnras/197.1.95

Antonucci, R. 1993, ARA&A, 31, 473, https://doi.org/10.1146/annurev.aa.31.090193.002353

Asplund, M., Grevesse, N., & Jacques Sauval, A. 2006, NuPhA, 777, 1, https://doi.org/10.1016/j.nuclphysa.2005.06.010

Baldwin, J., Ferland, G., Korista, K., & Verner, D. 1995, ApJ, 455, 119, https://doi.org/10.1086/309827

Baldwin, J. A., Ferland, G. J., Martin, P. G., Et al. 1991, ApJ, 374, 580, https://doi.org/10.1086/170146

Ballero, S. K., Matteucci, F., Ciotti, L., Calura, F., & Padovani, P. 2008, A&A, 478, 335, https://doi.org/10.1051/0004-6361:20078663

Baskin, A. & Laor, A. 2005, MNRAS, 358, 1043, https://doi.org/10.1111/j.1365-2966.2005.08841.x

Bennert, N., Jungwiert, B., Komossa, S., Haas, M., & Chini, R. 2006a, A&A, 459, 55, https://doi.org/10.1051/0004-6361:20065477

_____. 2006b, A&A, 456, 953, https://doi.org/10.1051/0004-6361:20065319

Binette, L. & Haro-Corzo, S. A. R. 2022, in prep.

Binette, L., Matadamas, R., Hägele, G. F., et al. 2012, A&A, 547, 29, https://doi.org/10.1051/0004-6361/201219515

Binette, L., Wang, J. C. L., Zuo, L., & Magris, C. G. 1993, AJ, 105, 797, https://doi.org/10.1086/116473

Binette, L., Wilson, A. S., Raga, A., & Storchi-Bergmann, T. 1997, A&A, 327, 909

Binette, L., Wilson, A. S., & Storchi-Bergmann, T. 1996, A&A, 312, 365

Boksenberg, A., Shortridge, K., Allen, D. A., et al. 1975, MNRAS, 173, 381, https://doi.org/10.1093/mnras/173.2.381

Boroson, T. A. & Green, R. F. 1992, ApJS, 80, 109, https://doi.org/10.1086/191661

Cameron, M., Storey, J. W. V., Rotaciuc, V., et al. 1993, ApJ, 419, 136, https://doi.org/10.1086/173467

De Robertis, M. M. & Osterbrock, D. E. 1984, ApJ, 286, 171, https://doi.org/10.1086/162585

_____. 1986, ApJ, 301, 727, https://doi.org/10.1086/163939

D'Odorico, S., Cristiani, S., Dekker, H., et al. 2000, SPIE 4005, Discoveries and Research Prospects from 8- to 10-Meter-Class Telescopes, ed. J. Bergeron, 121, https://doi.org/10.1117/12.390133

Dopita, M., Rhee, J., Farage, C., et al. 2010, Ap&SS, 327, 245, https://doi.org/10.1007/s10509-010-0335-9

Dopita, M. A., Scharwächter, J., Shastri, P., et al. 2014, A&A, 566, 41, https://doi.org/10.1051/0004-6361/201423467

Dors, O. L. Jr., Cardaci, M. V., Hägele, G. F., et al. 2015, MNRAS, 453, 4102, https://doi.org/10.1093/mnras/stv1916

Dors, O. L., Maiolino, R., Cardaci, M. V., et al. 2020, MNRAS, 496, 3209, https://doi.org/10.1093/mnras/staa1781

Feibelman, W. A. 2001, ApJ, 550, 785, https://doi.org/10.1086/319798

Ferguson, J. W., Korista, K. T., Baldwin, J. A., & Ferland, G. J. 1997, ApJ, 487, 122, https://doi.org/10.1086/304611

Filippenko, A. V. & Halpern, J. P. 1984, ApJ, 285, 458, https://doi.org/10.1086/162521

García-Rojas, J., Madonna, S., Luridiana, V., et al. 2015, MNRAS, 452, 2606, https://doi.org/10.1093/mnras/stv1415

Jackson, N. & Browne, I. W. A. 1991, MNRAS, 250, 422, https://doi.org/10.1093/mnras/250.2.422

Keel, W. C., de Grijp, M. H. K., Miley, G. K., & Zheng, W. 1994, A&A, 283, 791

Kewley, L. J., Nicholls, D. C., Sutherland, R., et al. 2019, ApJ, 880, 16, https://doi.org/10.3847/1538-4357/ab16ed

Korista, K., Baldwin, J., Ferland, G., & Verner, D. 1997, ApJS, 108, 401, https://doi.org/10.1086/312966

Koski, A. T. 1978, ApJ, 223, 56, https://doi.org/10.1086/156235

Kraemer, S. B., Crenshaw, D. M., Filippenko, A. V., & Peterson, B. M. 1998a, ApJ, 499, 719, https://doi.org/10.1086/305683

Kraemer, S. B., Ruiz, J. R., & Crenshaw, D. M. 1998b, ApJ, 508, 232, https://doi.org/10.1086/306389

Lawrence, A. 2012, MNRAS, 423, 451, https://doi.org/10.1111/j.1365-2966.2012.20889.x

Magris C., G., Binette, L., & Martin, P. 1993, Ap&SS, 205, 141, https://doi.org/10.1007/BF00657969

Maiolino, R., Marconi, A., & Oliva, E. 2001a, A&A, 365, 37, https://doi.org/10.1051/0004-6361:20000012

Maiolino, R., Marconi, A., Salvati, M., et al. 2001b, A&A, 365, 28, https://doi.org/10.1051/0004-6361:20000177

Martin, P. G. & Rouleau, F. 1991, A Selection of Papers Presented at the First Berkeley Colloquium on Extreme Ultraviolet Astronomy, ed. R. F. Malina, & S. Bowyer (New York, NY: Pergamon Press), 341

Meléndez, M., Kraemer, S. B., Armentrout, B. K., et al. 2008, ApJ, 682, 94, https://doi.org/10.1086/588807

Morganti, R., Robinson, A., Fosbury, R. A. E., et al. 1991, MNRAS, 249, 91, https://doi.org/10.1093/mnras/249.1.91

Mulchaey, J. S., Koratkar, A., Ward, M. J., et al. 1994, ApJ, 436, 586, https://doi.org/10.1086/174933

Murayama, T. & Taniguchi, Y. 1998, ApJ, 497, 9, https://doi.org/10.1086/311264

Murayama, T., Taniguchi, Y., & Iwasawa, K. 1998, AJ, 115, 460, https://doi.org/10.1086/300218

Nagao, T., Murayama, T., Shioya, Y., & Taniguchi, Y. 2002, ApJ, 575, 721, https://doi.org/10.1086/341355

Nagao, T., Murayama, T., & Taniguchi, Y. 2001, ApJ, 549, 155, https://doi.org/10.1086/319062

Netzer, H., Mainieri, V., Rosati, P., & Trakhtenbrot, B. 2006, A&A, 453, 525, https://doi.org/10.1051/0004-6361:20054203

Osterbrock, D. E. 1978, PhyS, 17, 285, https://doi.org/10.1088/0031-8949/17/3/024

Porter, R. L., Ferland, G. J., Storey, P. J., & Detisch, M. J. 2013, MNRAS, 433, 89, https://doi.org/10.1093/mnrasl/slt049

Rhee, J. H. & Larkin, J. E. 2005, ApJ, 620, 151, https://doi.org/10.1086/426884

Richardson, C. T., Allen, J. T., Baldwin, J. A., Hewett, P. C., & Ferland, G. J. 2014, MNRAS, 437, 2376, https://doi.org/10.1093/mnras/stt2056

Rodríguez-Ardila, A., Binette, L., Pastoriza, M. G., & Donzelli, C. J. 2000a, ApJ, 538, 581, https://doi.org/10.1086/309153

Rodríguez-Ardila, A., Pastoriza, M. G., & Donzelli, C. J. 2000b, ApJS, 126, 63, https://doi.org/10.1086/313293

Rose, M., Elvis, M., Crenshaw, M., & Glidden, A. 2015a, MNRAS, 451, 11, https://doi.org/10.1093/mnrasl/slv056

Rose, M., Elvis, M., & Tadhunter, C. N. 2015b, MNRAS, 448, 2900, https://doi.org/10.1093/mnras/stv113

Storchi-Bergmann, T. & Pastoriza, M. G. 1990, PASP, 102, 1359, https://doi.org/10.1086/132775

Storchi-Bergmann, T., Wilson, A. S., Mulchaey, J. S., & Binette, L. 1996, A&A, 312, 357

Tadhunter, C. N., Fosbury, R. A. E., Binette, L., Danziger, I. J., & Robinson, A. 1987, Natur, 325, 504, https://doi.org/10.1038/325504a0

Tadhunter, C. N., Fosbury, R. A. E., di Serego Alighieri, S., et al. 1988, MNRAS, 235, 403, https://doi.org/10.1093/mnras/235.2.403

Tadhunter, C. N., Metz, S., & Robinson, A. 1994, MNRAS, 268, 989, https://doi.org/10.1093/mnras/268.4.989

Villar Martín, M., Bellocchi, E., Stern, J., et al. 2015, MNRAS, 454, 439, https://doi.org/10.1093/mnras/stv1864

Villar-Martín, M., Emonts, B., Cabrera Lavers, A., et al. 2017, MNRAS, 472, 4659, https://doi.org/10.1093/mnras/stx2209

Villar-Martín, M., Humphrey, A., Martínez-Sansigre, A., et al. 2008, MNRAS, 390, 218, https://doi.org/10.1111/j.1365-2966.2008.13779.x

York, D. G., Adelman, J., Anderson, J. E., et al. 2000, AJ, 120, 1579, https://doi.org/10.1086/301513

A. Alarie: Département de physique, de génie physique et d'optique, Université Laval, Québec, QC G1V 0A6, Canada.
L. Binette: Instituto de Astronomía, Universidad Nacional Autónoma de México, A.P. 70-264, Ciudad de México, C. P. 04510, México,
G. Magris: Centro de Investigaciones de Astronomía, Apartado Postal 264, Mérida 5101-A, Venezuela
M. Martínez-Paredes: Korea Astronomy and Space Science Institute 776 Daedeokdae-ro, Yuseong-gu, Daejeon, 34055, Republic of Korea.
A. Rodríguez Ardila: Laboratório Nacional de Astrofísica - Rua dos Estados Unidos 154, Bairro das Nações. CEP 37504-364, Itajubá, MG, Brazil.
M. Villar-Martín: Centro de Astrobiología, (CAB, CSIC-INTA), Departamento de Astrofísica, Cra. de Ajalvir Km. 4, 28850, Torrejón de Ardoz, Madrid, Spain.
I. Villicaña-Pedraza: DACC Science Department, New Mexico State University, Las Cruces, NM 88003, USA.